PFG – Journal of Photogrammetry, Remote Sensing and Geoinformation Science
https://doi.org/10.1007/s41064-025-00375-6

ORIGINAL ARTICLE

Estimation of Incidence Angles and Ranging Accuracy via Simulation of Full-Waveform LiDAR

Jan Rhomberg-Kauert[1] · **Florian Pöppl**[1,2] · **Lucas Dammert**[1] · **Martin Pfennigbauer**[3] · **Gottfried Mandlburger**[1]

Received: 2 September 2025 / Accepted: 26 December 2025

Abstract

Topo-bathymetric LiDAR has become a standard 3D geodata acquisition technique in geosciences with a wide range of applications in terrestrial and aquatic landscapes. In particular, the usage of short laser pulses with medium-sized footprints for bathymetric applications has seen growing attention over the past decade. These LiDAR configurations have shown higher relative changes in echo pulse width in relation to angle of incidence compared to standard topographic LiDAR using more collimated near-infrared lasers. Although angle-dependent changes in amplitude have been well documented, quantification of such a relation for the echo pulse width is still not entirely solved. By focusing on LiDAR with short and broad pulses, we can therefore use the higher relative changes of such systems together with numerical simulations to quantify the relationship between the echo pulse width and the angle of incidence. The simulation developed in this study can be used to estimate neighborhood-independent angles of incidence from the recorded waveform, which enables the angle of incidence calculation during waveform processing. These waveform-derived angles are comparable to established methods based on the local point neighborhood, but generally display a higher variance leading to a mean absolute error of about 10° when compared to neighborhood-based angles of incidence. Using the developed simulation, we also explore angle-dependent shifts of the peak amplitude linked to potential ranging offsets. There, we were able to show ranging offsets of up to 12 cm for strongly asymmetric laser pulses at angles of 80° and no offsets for symmetric laser pulses, which provides new insights into the correctness of topo-bathymetric LiDAR systems. In conclusion, we present a detailed simulation framework which can be used to estimate incidence angles and quantify potential ranging offsets.

Keywords Incidence angles · Echo pulse width · Signal processing · Peak detection · Gaussian fitting · Heavy-tailed curve

1 Introduction

Light Detection and Ranging (LiDAR) has a long history of application in different fields of research related to mapping of natural habitats and man-made structures (Nelson 2013; Ullrich et al. 2007; Mandlburger 2020). Both terrestrial and airborne laser scanning (TLS and ALS) systems have seen significant improvements in the last decades, reducing costs and increasing possible applications (Ullrich et al. 2007; Mandlburger et al. 2023). Advances in signal processing have improved data quality (Li and Ibanez-Guzman 2020; Pfennigbauer et al. 2014) and the increasing usage of unmanned aerial vehicles (UAVs) has made ALS accessible to a broader audience (Mandlburger et al. 2011; Pfennigbauer and Ullrich 2011). Bathymetric LiDAR, suitable for the penetration of water bodies, almost exclusively uses a wavelength of 532 nm, while topographic LiDAR usually uses near-infrared (NIR) lasers (e.g., 1064 nm) (Mallet and Bretar 2009; Mandlburger 2020; Pfennigbauer and Ullrich

---

✉ Jan Rhomberg-Kauert
jan.rhomberg-kauert@geo.tuwien.ac.at

Florian Pöppl
florian.poeppl@geo.tuwien.ac.at

Lucas Dammert
lucas.dammert@geo.tuwien.ac.at

Martin Pfennigbauer
mpfennigbauer@riegl.com

Gottfried Mandlburger
gottfried.mandlburger@geo.tuwien.ac.at

[1] Department of Geodesy and Geoinformation, TU Wien, 1040 Vienna, Austria

[2] RIEGL Laser Measurement Systems GmbH, 3580 Horn, Austria

[3] RIEGL Research and Defense GmbH, 3580 Horn, Austria

2011). In addition, there are differences in pulse width and footprint size depending on the requirements of the survey or the sensor (Mandlburger et al. 2011, 2023). For bathymetric LiDAR, the clear separation of points from the water surface and shallow bottom requires (i) short pulses and (ii) a relatively larger laser footprint (Mandlburger et al. 2011; Williams 2017). The latter is a direct consequence of general regulations related to eye safety. In contrast, the typical NIR LiDAR has longer pulses and a smaller footprint.

For both systems, the introduction of full-waveform LiDAR, where the entire temporal history of the reflected laser pulse is recorded (Li and Ibanez-Guzman 2020; Mallet and Bretar 2009; Ullrich et al. 2007; Ullrich and Pfennigbauer 2011), has enabled additional signal processing that extends from onboard analysis and opens up the possibility to analyze the data in more detail in post-processing (Mallet and Bretar 2009; Pfennigbauer et al. 2013, 2014). For topo-bathymetric LiDAR, the processing of full-waveform data has become a standard tool to improve the detection of underwater echoes (Schwarz et al. 2019) or, more generally, to improve the extraction of target positions from the reflected signal (Allouis et al. 2010; Pfennigbauer et al. 2013, 2014).

To determine the return time of the reflected echo pulse, several methods exist, including leading-edge detection, peak detection, center-of-gravity methods, and fitting of idealized pulse shapes (such as a Gaussian pulse) to the recorded data (Li et al. 2018; Schwarz et al. 2017; Ullrich and Pfennigbauer 2011; Wagner 2010). Focusing on standard processing, the extraction of the target from the recorded samples through peak detection or Gaussian fitting has been established for a wide range of applications (Pfennigbauer et al. 2014; Wagner 2010). As the Gaussian pulse represents an idealized echo pulse, which is symmetrical, additional methods have explored asymmetric pulses (Chauve et al. 2007; Ji et al. 2022; Rhomberg-Kauert et al. 2024; Wang et al. 2015). The application of these asymmetric pulses during echo extraction aims to better capture the differences between the rising and falling edges of the echo pulse (Ma et al. 2024). There, depending on the inclination and reflective properties of the target surface, the asymmetric pulse displays a stronger temporal shift of the maximum amplitude compared to symmetric functions (Hu et al. 2022), which in turn can influence the calculation of range and reflectance.

For full-waveform LiDAR, the relationship between signal amplitude and echo pulse width has long been established, as these parameters are directly related to the reflected optical energy (Wagner et al. 2006). There, the relationship between the angle of incidence and the amplitude is described through the Lambertian-Cosine law, for ideally diffuse reflecting targets (Guo et al. 2023). The angle of incidence is defined as the angle between the direction of the laser beam and the surface normal direction. Furthermore, the influence of the angle of incidence on the overall waveform has been well researched (Kaasalainen et al. 2011; Kukko et al. 2008; Li et al. 2018). An increasing angle of incidence is associated with a decrease in ranging correctness (Kukko et al. 2008). In contrast, for the dependency of echo pulse width and angle of incidence, a relation was observed mainly at high angles for simulation based work (Bolkas 2019; Kukko et al. 2008; Yang et al. 2021). Under real-world conditions, no clear relation was observed (Pfennigbauer et al. 2013). Thus, current methods for determining the angle of incidence are mainly based on information from neighboring 3D points and calculated during post-processing of LiDAR data (Pfeifer et al. 2014).

Neighborhood information can, for example, be extracted using the scientific laser scanning software OPALS (Pfeifer et al. 2014), where normal vectors are calculated based on planes fitted to neighboring points. Thus, the angle of incidence is calculated using the normal vector and the laser beam vector (Pfeifer et al. 2014). The disadvantage of such a neighborhood-based method is that the input parameters often need fine-tuning to achieve optimal results, which limits automation and requires substantial time in post-processing of the dataset.

This highlights the challenges in extracting the angles of incidence and the far-reaching impact they have on the research based on LiDAR signal processing (Kaasalainen et al. 2011; Kukko et al. 2008; Pfennigbauer et al. 2013). Therefore, this study extends existing work through the introduction of a full-waveform simulation based on Carlsson et al. (2001). Our simulation framework allows us to analyze the interaction of an echo pulse with inclined extended scattering objects in detail and uses the gained insight to model the relation between the echo pulse width and the angle of incidence. The derived angles can then be compared with current state-of-the-art methods, such as neighborhood-based angle of incidence calculation with the OPALS laser scanning software (Pfeifer et al. 2014). Here, the comparison focuses on airborne LiDAR data and uses a TLS dataset for additional validation. Furthermore, the simulation framework provides a basis for the theoretical investigation of the influence of the angle of incidence on the temporal position of the maximum amplitude. This relation can then be analyzed for different degrees of waveform model asymmetry, ranging from heavy-tailed curves to symmetrical Gaussian pulses and provides insight into a possible ranging bias for inclined targets.

The primary objective of our study is to simulate the interaction of the laser pulse with inclined targets. Based on this simulation, two topics of interest can be defined: (i) the relationship between the echo pulse width and the angle of incidence and how the relation between the two quantities can be used to estimate neighborhood-independent angles of incidence, and (ii) the analysis of temporal shifts of the maximum amplitude through angled targets and how waveform symmetry influences the detected shifts. Both topics are investigated by developing a simulation framework (Sect. 4.1) that enables analysis of the full waveform in high temporal resolution (Sect. 4.2), followed by establishing a relationship between the echo pulse width and the angle of incidence (Sect. 4.3). The evaluation metrics for the angle of incidence estimation are given in Sect. 4.4. Furthermore, this study simulates the effects of asymmetric laser pulses and their interaction with angled surfaces (Sect. 4.5), introduces a method to compare the simulation and real-world data (Sect. 4.6), and analyzes the influence of the angle of incidence on the temporal position of the peak, that is, the range accuracy (Sect. 4.7). The results of the simulation framework are then compared with current state-of-the-art processing and real-world data (Sect. 5). Lastly, we critically discuss and compare our results with established research (Sect. 6).

2 Theoretical Basis of Full-waveform LiDAR

Full-waveform LiDAR can be described using the mathematical parameters influencing the interaction of the emitted laser pulse and the backscatter cross section of the target (Wagner 2010). For the subsequent simulation of this interaction (Sect. 4), this section first introduces the mathematical notation used (Sect. 2.1) and outlines the fundamental differences between the typical green and NIR laser pulses as used in this study (Sect. 2.2).

Table 1 Variables used throughout the paper.

Symbol	Equation	Description
c	–	Speed of light [m/s]
t	–	Return trip time [s]
R	$R = \frac{1}{2} c \cdot t$	Range [m]
τ	–	Echo pulse width at standard deviation [ns]
$T_{e^{-2}}$	$\tau = \frac{T_{e^{-2}}}{4}$	Echo pulse width at e^{-2} [ns]
$T_{1/2}$	$\tau = \frac{T_{1/2}}{2 \cdot \sqrt{2 \log(2)}}$.	Full Width at Half Maximum [ns]
θ	–	Beam divergence [mrad]
α	–	Angle of incidence [°]
r_0	–	Footprint radius at $R = 0$ [m]
$\mathcal{F}_0$	$\mathcal{F}_0 = \frac{1}{2} \sqrt{(\theta \cdot R)^2 + r_0^2}$	Footprint radius measured at $1/e^2$ at target [m]
$\mathcal{F}_\alpha$	$\mathcal{F}_\alpha = \frac{\mathcal{F}_0}{\cos(\alpha)}$	Semi-major axis (Ellipse) [m]
$g(t)$	Equation 2	Gaussian pulse
$f(t)$	Equation 3	Heavy-tailed curve
$\mathcal{P}$	$p \in \mathcal{P}$	The set of all LiDAR points

2.1 Mathematical Notation

The mathematical notations used in this document are listed in Table 1 together with a brief description, including the units of measurement. On this basis, we present the employed equations.

2.2 Differences of the Emitted Pulse

The fundamental working principles of time-of-flight LiDAR can be characterized by the following equation (Synge 1930):

$$R = \frac{1}{2} c \cdot t \tag{1}$$

Here, R is the range from the laser scanner to the target, c is the speed of light (group velocity), and t is the return trip time. In full-waveform LiDAR, the entire reflected waveform is also recorded, in addition to the target range. This waveform is affected by both the footprint size at the target and the emitted laser pulse length, as well as the backscatter cross section of the target. For example, NIR LiDAR often uses long pulses measured at full width half maximum (FWHM) with a small footprint ($\mathcal{F}_0$), while bathymetric (green) LiDAR commonly uses short pulses and a medium-sized footprint (Fig. 1a and c). The footprint radius $\mathcal{F}_0$ for non-inclined targets refers to a circular footprint at distance R from the laser scanner, while for inclined targets the footprint is elliptical, where the semi-minor axis still corresponds to $\mathcal{F}_0$ and the elongated axis (the semi-major axis) in beam direction is given by $\mathcal{F}_\alpha$.

The beam divergence θ is either fixed or can be set before data acquisition, depending on the system used. However, the echo pulse width and amplitude depend on angle of incidence (Wagner 2010). This is schematically illustrated in Fig. 1. For the two types of airborne LiDAR systems, we can distinguish two categories: (i) LiDAR with short pulses and medium-sized footprints, for example typical topo-bathymetric (green) LiDAR and (ii) long pulses and small footprints, e.g. commonly used in topographic (NIR) LiDAR. This difference in laser pulse shape of the two LiDAR systems leads to a difference in the relative change after interacting with an inclined target. For typical NIR LiDAR systems, this means that the relative change of the echo pulse width is small for most observed angles.

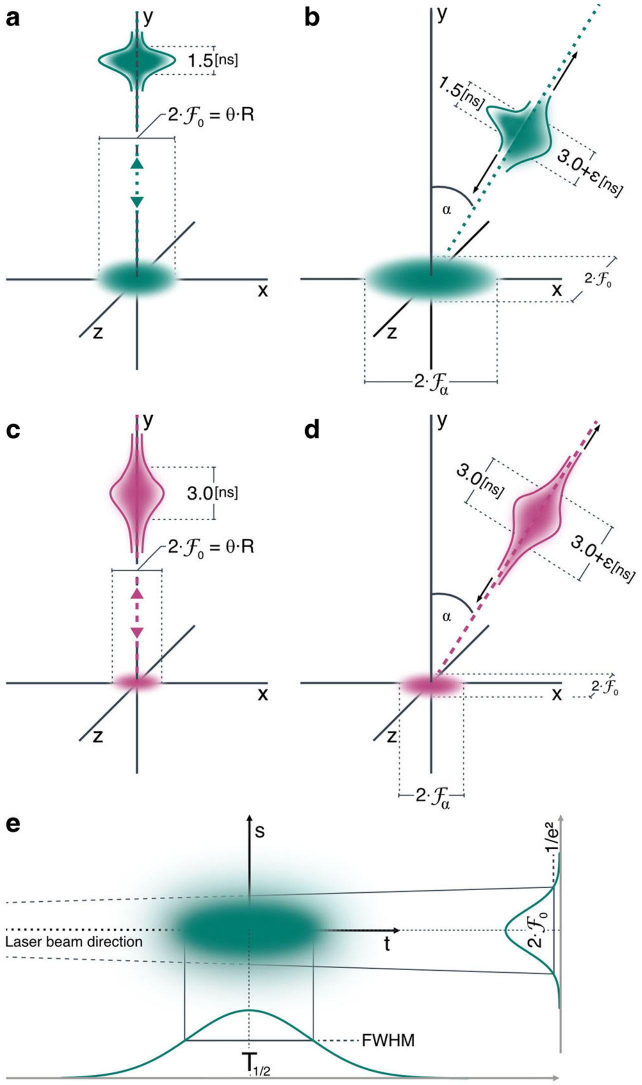

Fig. 1 (**a–d**) Illustration of the differences in pulse width (left side, emitted laser pulse) and echo pulse width (right side, reflected laser pulse) depending on the LiDAR system with a footprint radius $\mathcal{F}_0$ and semi-major axis $\mathcal{F}_\alpha$, after interacting with a Lambertian reflector. Furthermore the angle α is greater or equal to 60° in panels **b** and **d**, so that the pulse length holds true for $\varepsilon > 0$. Panel **e** displays the model used to describe a general laser pulse, illustrating the different parameters affecting the pulse width at FWHM ($T_{1/2}$) and footprint diameter ($2F_0$) measured at $1/e^2$ of the laser pulse, which are further explained in Table 1.

In contrast, for typical green LiDAR systems, the shorter pulses and larger footprints lead to greater changes in the echo pulse width. This can be observed, for example, in the difference of reflectance on differently sloped roofs. The differences in footprint size and pulse width become noticeable because at angled targets parts of the pulse are reflected at a later point in time (farther away in beam direction). Thus, the absolute increase in length is more noticeable for shorter pulses, as here even small changes lead to larger relative changes (Laconte et al. 2019).

The changes in laser pulse width and amplitude are common for bathymetric LiDAR, but in fact the difference in relative change after interaction with an angled target is not attributed to the laser wavelength but to the illuminated surface (footprint at ground level) and pulse length (FWHM).

3 Materials

To set up the simulation framework, this section introduces the study area (Sect. 3.1) and presents the data sets used to validate the angle estimation with current best practices (Sect. 3.2).

3.1 Study Area

The surveyed area is located in Loosdorf (48.2010° N, 15.4004° E; WGS 84) in Lower Austria. The region contains a variety of structures with different orientations, mainly houses with tilted roofs (Fig. 1), which can be used to evaluate our estimation of the angle of incidence. For the selected area of interest, three different datasets (one terrestrial multi-scan-positions and two topo-bathymetric airborne LiDAR datasets) are available that build a comprehensive foundation for the comparison of the angle of incidence estimation. The focus on a topographic landscapes provides the additional advantage of roofs where material and backscatter characteristics should be predominantly uniform for a single roof, while in aquatic landscapes refraction, water surface interaction and water column backscatter would influence the waveforms and thus lead to less conclusive results.

Table 2 The properties of the two LiDAR systems deployed during the data acquisition. For each system the following parameters are given: the wavelength λ, beam divergence θ, footprint diameter measured at $1/e^2$ at ground level $2\mathcal{F}_0$ (without inclination) and the FWHM of the emitted laser pulse $T_{1/2}$.

System	λ [nm]	θ [mrad]	$2\mathcal{F}_0$ [m]	$T_{1/2}$ [ns]
Sensor I	532	0.9	0.4–0.7	1.5
Sensor I	1064	0.3	0.1–0.2	3.0
Sensor II	532	1.0	0.6–1.0	1.5
Sensor II	1064	0.2	0.1–0.3	3.0

3.2 LiDAR Data

The two main airborne data sets for this study were acquired with the *RIEGL* VQ-880-GII topo-bathymetric (dual-wavelength; NIR and green LiDAR) laser scanner (Sensor I) and the *RIEGL* VQ-1560i-DW dual-wavelength laser scanner (Sensor II). For each system, the parameters of the individual laser channels are shown in Table 2. The main difference between the green channels of both systems is that Sensor I has a constant off-nadir angle of 20° (*RIEGL*, Laser Measurement Systems 2022b), resulting in a circular scan pattern on the ground, while Sensor II acquires a pair of parallel straight scan lines approximately orthogonal to the flight direction with an angular offset of ±14° (*RIEGL*, Laser Measurement Systems 2022a). The off-nadir angles vary between ±30° (Fig. 2).

The scan parameters, such as the wavelength λ, beam divergence θ, $1/e^2$ footprint diameter at ground level $2\mathcal{F}_0$, and the Full Width at Half Maximum (FWHM) of the amplitude $T_{1/2}$, are shown in Table 2. Another important property of the LiDAR system is the waveform sampling interval, which amounts to 0.58 ns for Sensor I and 1.01 ns for Sensor II, for the green channel, respectively. Furthermore, for the green channel datasets, the pulse repetition rate differs; the Sensor I dataset was acquired with a pulse repetition rate of 200 kHz, and the Sensor II dataset with 700 kHz. Both scanners support full-waveform recording, allowing for the extraction of the returned echo pulses for each waveform based on the stored waveform samples. In addition to the airborne data sets, a ground-based multi-scan-position data set of the roofs (Fig. 3c) was acquired. The TLS used for the stationary measurements was a *RIEGL* VZ-600i laser scanner mounted on a tripod. This setup was used for the multiple scan positions around the house shown in Fig. 3c, acquiring a high resolution terrestrial point cloud of the roof. The goal of this data set is to provide a much denser point cloud compared to airborne data sets, which allows the calculation of neighborhood-based angles of incidence using a high-resolution dataset, thus improving the quality of the calculated angles.

4 Method

The method of estimating the angle of incidence is based on a simulation of the full-waveform data. First, we present the emitted waveforms that are used as input for the simulation in Sect. 4.1, initially a gaussian pulse and a heavy-tailed curve. Second, the impulse response of the angled plane (differential backscatter cross section) is described in Sect. 4.2. The functions are then convolved and the generated output is used to establish a relationship between the angle of incidence and the echo pulse width (Sects. 4.3 and 4.4). Lastly, the analysis is extended by additional waveforms with varying degrees of symmetry between the heavy-tailed curve and the gaussian pulse to analyze the effect of laser pulse symmetry and angle of incidence on the temporal position of the waveform maximum (Sect. 4.5–4.7).

4.1 Initial System Waveform

To model the initial waveforms sent out by the laser scanner, a number of suitable functions exist, ranging from a Gaussian pulse model to more specific functions that more accurately reflect the actual laser waveform characteristics. For

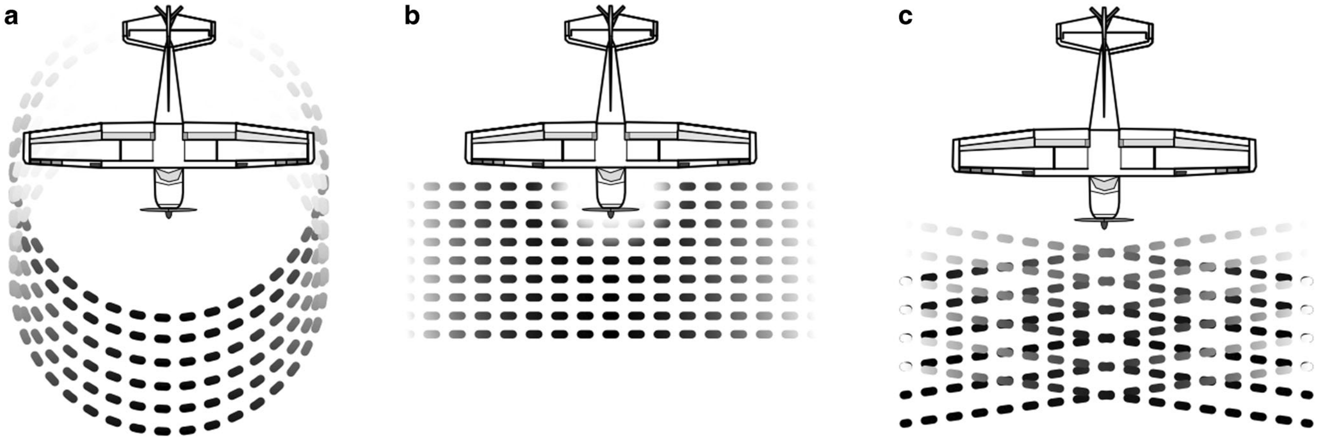

Fig. 2 **a** Illustration of the circular scan pattern of the green channel of Sensor I with a constant off-nadir angle of 20°. **b** Linear scan pattern of the NIR channel of Sensor I **c** Linear scan pattern of Sensor II.

Fig. 3 **a** Map of the study area in Loosdorf, Lower Austria (Bundesamt für Eich- and Vermessungswesen 2024), where the first dataset (**b**) is marked with B and the second (**c**) with C. In contrast to the first dataset (**b**), which only consists of airborne LiDAR data, the second dataset (**c**) was surveyed with both airborne and terrestrial LiDAR; the latter as an additional reference.

the simulation in this paper, we use two initial functions: a Gaussian pulse (Fig. 4a) given by

$$g(t) = e^{\frac{-t^2}{2\tau^2}}, \tag{2}$$

and a heavy-tailed function (Fig. 4b) as defined by Carlsson et al. (2001),

$$f(t) = \begin{cases} \left(\frac{t}{\tau}\right)^2 e^{-\frac{t}{\tau}} & t \geq 0 \\ 0 & \text{otherwise.} \end{cases} \tag{3}$$

There, τ is given by

$$\tau = \frac{T_{e^{-2}}}{4} = \frac{T_{1/2}}{2\sqrt{2\log(2)}}. \tag{4}$$

Both functions exhibit individual characteristics, and they differ mainly in the degree of asymmetry observed after the signal peak. Compared to the commonly used Gaussian model, the heavy-tailed curve better captures the slightly asymmetric shapes of actual laser pulses. However, the Gaussian model is more commonly used and represents an idealized pulse shape. This allows us to account for the impact of asymmetry in our analysis of the different waveforms. Thus, the introduction of both functions creates a more versatile simulation framework.

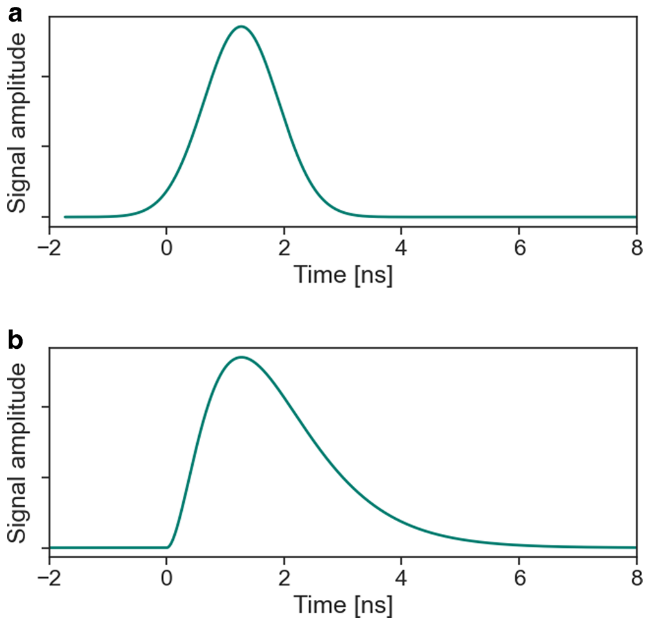

Fig. 4 **a** Gaussian pulse $g(t)$ and **b** heavy-tailed curve $f(t)$ with $T_{1/2} = 1.5$ ns and thus τ as shown in Eq. 4.

4.2 Waveform Simulation

For the pulse interaction with an inclined target, we enhance the simulation framework of Carlsson et al. (2001) with a new parameterization. This previous work develops a framework of laser beam propagation theory, which uses a heavy-tailed curve $f(t)$ (Fig. 4a) and an angle-dependent function to compute the interaction of a laser pulse with an angled target. We use the angle-dependent function defined

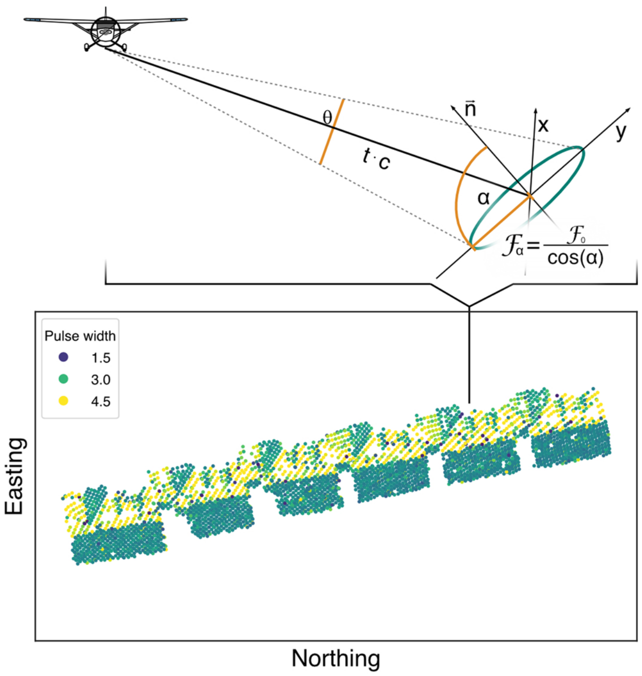

Fig. 5 Illustration of parameters in the simulation framework for an inclined LiDAR footprint. The parameters of the elliptical LiDAR footprint are highlighted by the orange semi-major axis $\mathcal{F}_\alpha$, outlining the assumed geometry for the angled surfaces shown in the top-down view of the point cloud below.

by Carlsson et al. (2001) and adapt the pulse-target interaction to the geometry of airborne laser scanning as shown in Fig. 5. The angle-dependent function $h(t, \alpha)$ is defined through Eq. 5, taking into account the incidence angle and footprint size in the x-y-plane. In Eq. 5, the interaction and the illuminated area of the laser pulse are given as a convolution, with δ being the Dirac delta function.

$$h(t, \alpha) = \int_{-\infty}^{\infty} \int_{-\infty}^{\infty} e^{\frac{-x^2}{\mathcal{F}_\alpha^2} + \frac{-y^2}{\mathcal{F}_0^2}} \cdot \delta \left(t - \frac{\sin(\alpha) x}{c} \right) dx\, dy. \tag{5}$$

Here, $\mathcal{F}_\alpha$ is the semi-major axis of the footprint, c is the speed of light, and α denotes the angle of incidence. The angle is defined so that $\alpha = 0$ when the surface normal vector and the laser beam vector coincide. By choosing the following substitution

$$\tilde{x} = -\frac{\sin(\alpha) x}{c} \quad \Leftrightarrow \quad x = -\frac{c \cdot \tilde{x}}{\sin(\alpha)}, \tag{6}$$

we can rewrite the previous integral of Eq. 5 using the new parameterization, so that later the translation property of the Dirac delta can be used to simplify the integral.

$$\begin{aligned} h(t, \alpha) = & \int_{-\infty}^{\infty} \int_{-\infty}^{\infty} e^{\frac{-x^2}{\mathcal{F}_\alpha^2} + \frac{-y^2}{\mathcal{F}_0^2}} \cdot \delta \left(t - \frac{\sin(\alpha) x}{c} \right) \\ & \left(-\frac{c}{\sin(\alpha)} \right) \cdot \left(-\frac{\sin(\alpha)}{c} \right) dx\, dy. \end{aligned} \tag{7}$$

$$\begin{aligned} = & -\frac{c}{\sin(\alpha)} \int_{-\infty}^{\infty} \lim_{x \to \infty} \int_{-\left(-\frac{\sin(\alpha) x}{c}\right)}^{-\frac{\sin(\alpha) x}{c}} e^{-\frac{1}{\mathcal{F}_\alpha^2} \cdot \left(\frac{c \tilde{x}}{\sin(\alpha)} \right)^2} \\ & \cdot e^{-\frac{y^2}{\mathcal{F}_0^2}} \cdot \delta \left(\tilde{x} - (-t) \right)\, d\tilde{x}\, dy \end{aligned} \tag{8}$$

$$\begin{aligned} = & -\frac{c}{\sin(\alpha)} \int_{-\infty}^{\infty} \int_{\infty}^{-\infty} e^{-\frac{1}{\mathcal{F}_\alpha^2} \cdot \left(\frac{c \tilde{x}}{\sin(\alpha)} \right)^2} \\ & \cdot e^{-\frac{y^2}{\mathcal{F}_0^2}} \cdot \delta \left(\tilde{x} - (-t) \right)\, d\tilde{x}\, dy \end{aligned} \tag{9}$$

$$\begin{aligned} = & \frac{c}{\sin(\alpha)} \int_{-\infty}^{\infty} \int_{-\infty}^{\infty} e^{-\frac{1}{\mathcal{F}_\alpha^2} \cdot \left(\frac{c \tilde{x}}{\sin(\alpha)} \right)^2} \\ & \cdot e^{-\frac{y^2}{\mathcal{F}_0^2}} \cdot \delta \left(\tilde{x} - (-t) \right)\, d\tilde{x}\, dy \end{aligned} \tag{10}$$

By definition, we know that $\mathcal{F}_\alpha = \frac{\mathcal{F}_0}{\cos(\alpha)}$, and thus we get

$$-\left(\frac{c \tilde{x}}{\mathcal{F}_\alpha \sin(\alpha)} \right)^2 = -\left(\frac{c \tilde{x}}{\frac{\mathcal{F}_0}{\cos(\alpha)} \sin(\alpha)} \right)^2 = -\left(\frac{c \tilde{x}}{\mathcal{F}_0 \tan(\alpha)} \right)^2.$$

The utilization of this transformation, applied to $h(t, \alpha)$ together with the translation property of the Dirac delta function then yields

$$\begin{aligned} h(t, \alpha) = & \frac{c}{\sin(\alpha)} \int_{-\infty}^{\infty} e^{-\frac{y^2}{\mathcal{F}_0^2}} \int_{-\infty}^{\infty} e^{-\left(\frac{c \tilde{x}}{\mathcal{F}_\alpha \sin(\alpha)} \right)^2} \\ & \cdot \delta \left(\tilde{x} - (-t) \right)\, d\tilde{x}\, dy \end{aligned} \tag{11}$$

$$= \frac{c}{\sin(\alpha)} \cdot e^{-\left(\frac{ct}{\mathcal{F}_0^2 \tan(\alpha)} \right)^2} \int_{-\infty}^{\infty} e^{-\frac{y^2}{\mathcal{F}_0^2}}\, dy \tag{12}$$

$$= \frac{c}{\sin(\alpha)} \cdot e^{-\left(\frac{ct}{\mathcal{F}_0^2 \tan(\alpha)} \right)^2} \cdot \sqrt{\pi} \mathcal{F}_0. \tag{13}$$

Furthermore, we multiply Eq. 13 with $\cos(\alpha)$ to account for the change in amplitude of a Lambertian reflector, as the amplitude is also an angle-dependent quantity (Hartzell et al. 2015). This improves the visual comparison of the different waveforms but does not have a direct influence on the width calculation later on. Ultimately, we get:

$$\tilde{h}(t,\alpha) = \cos(\alpha)\cdot h(t,\alpha) \tag{14}$$

$$\begin{aligned} &= \cos(\alpha)\cdot \frac{c}{\sin(\alpha)}\cdot e^{-\left(\frac{ct}{\mathcal{F}_0 \tan(\alpha)}\right)^2}\cdot \sqrt{\pi}\mathcal{F}_0 \\ &= \frac{c\cdot\sqrt{\pi}\mathcal{F}_0}{\tan(\alpha)}\cdot e^{-\left(\frac{ct}{\mathcal{F}_0 \tan(\alpha)}\right)^2}. \end{aligned} \tag{15}$$

We can now simulate the received full-waveform $f_{\text{reflected}}(t,\alpha)$ for each angle. The received full-waveform is therefore defined as the convolution of the initial pulse $f(t)$ and the differential backscattering cross section for the angled target $\tilde{h}(t,\alpha)$. This convolution is given by the following equation, where ξ is the variable of the convolution:

$$f_{\text{reflected}}(t,\alpha) = \left(f * \tilde{h}\right)(t,\alpha) \tag{16}$$

$$= \int_0^t f(\xi)\cdot \tilde{h}(t-\xi,\alpha)\, d\xi. \tag{17}$$

4.3 Angle Estimation

Based on the simulation framework introduced above, we can now present a method that estimates the angle of incidence based on the width of the echo pulse. For this, we create a simulated curve between the echo pulse width measured from the simulated waveforms and the angle of incidence. The simulated echo pulse (Eq. 17) can be evaluated at $T_{e^{-2}}$ for each input angle and converted to FWHM (Eq. 4). We calculate the echo pulse width from the recorded laser waveform as the FWHM based on Gaussian decomposition (Ullrich and Pfennigbauer 2011), as this is a standard full-waveform processing technique.

For the general application of this newly introduced method, some limitations of the data have to be considered to avoid wrong matching between width and angle of incidence. The two main constraints are that (i) the echo pulse width is within the range of the corresponding simulated curve and that (ii) the extracted width corresponds only to a single return pulse. To address the prior, a threshold is set for the minimum width of the simulated curve for each data set. If the echo pulse widths are below that threshold, no angle of incidence is assigned for this point, as the angle would incorrectly be zero. The latter constraint is the consideration of single returns only. The methodology is only applicable for fully illuminated targets, i.e., the laser footprint completely covers a single object.

To later compare this new method with current best practices regarding angle-of-incidence calculation, we introduce the respective workflows here. For this, we use the point cloud processing software OPALS (Pfeifer et al. 2014). There, the module *opalsNormals* is used to estimate the 3D surface normal vectors of the illuminated laser spots based on locally neighboring points. We define the neighborhood as follows: k-nearest neighbors (k = 32) and quadrant-wise point selection, i.e, the 8 nearest neighbor points are selected in each quadrant around the LiDAR point. We estimate the normal vectors using a robust plane fitting approach, which detects and eliminates outliers within a robust least squares adjustment framework. These normal vectors can then be combined with the laser beam vectors, derived from the flight trajectory, to calculate the angle of incidence. This provides a neighborhood-based angle of incidence for each point in the point cloud and can be compared to the waveform-based angles in Sect. 5.

4.4 Evaluation Metrics

In the following, we introduce the metrics used for the qualitative evaluation of the incidence angles derived from the echo pulse width. For this, let α^{wfm} and α^{nbr} be the angle of incidence calculated using our waveform-based and standard neighborhood-based methods, where $n \in \mathbf{N}$ is the number of incidence angles calculated. Then the point-wise difference in angles is defined as

$$\Delta(\alpha_i) = \alpha_i^{\text{nbr}} - \alpha_i^{\text{wfm}} \text{ for } 0 \le i \le n. \tag{18}$$

With this, we can define the following different evaluation metrics

$$\text{AD} = \frac{1}{n}\sum_{i=1}^{n} \Delta(\alpha_i) \tag{19}$$

$$\text{MD} = \text{median}_i\ \Delta(\alpha_i) \tag{20}$$

$$\text{AAE} = \frac{1}{n}\sum_{i=1}^{n} |\Delta(\alpha_i)| \tag{21}$$

$$\text{MAE} = \text{median}_i\ |\Delta(\alpha_i)|. \tag{22}$$

The used acronyms are Average Difference (AD), Median Difference (MD), Average Absolute Error (AAE) and Median Absolute Error (MAE).

4.5 Simulating Degree of Asymmetry in the Initial Laser Pulse

The simulation based on the heavy-tailed curve of Carlsson et al. (2001) reflects only one of many possible waveforms, which can be used to approximate the initial waveform. For this reason, we broadened our analysis to include a selection of different waveforms, ranging from a symmetric Gaussian pulse to the asymmetrical heavy-tailed curve introduced previously. With the Gaussian pulse $g(t)$ as defined by Eq. 2, we can calculate the convolution $g_{\text{reflected}}(t,\alpha)$ of the Gaussian pulse $g(t)$ with the angle-dependent function $\tilde{h}(t, \alpha)$, given by

$$g_{\text{reflected}}(t, \alpha) = \left(g * \tilde{h}\right)(t, \alpha) \tag{23}$$

$$= \int_0^t g(\xi) \cdot \tilde{h}(t - \xi, \alpha)\, d\xi. \tag{24}$$

This can also be extended to a range of functions in between the Gaussian pulse and the heavy-tailed curve by introducing homotopy (Arkowitz 2011). We define the continuous homotopy function from the Gaussian pulse to the heavy-tailed curve as:

$$\begin{aligned} H &: [0,1] \times \mathbb{R} \to \mathbb{R}, \\ &H(s,t) \mapsto s \cdot f(t) + (1-s) \cdot g(t). \end{aligned} \tag{25}$$

The generated spectrum of functions, created by the homotopy for the parameter $s \in [0, 1]$, can now be applied as the initial waveform, serving as the basis for the convolution with the angle-dependent function. This allows for the analysis of potential ranging effects caused by shifts of the maximum peak.

4.6 Waveform Averaging and Curve Fitting

In order to verify the overall alignment of the selected waveforms for the simulation with real-world data, and to provide a basis for the later discussion, this section presents the topic of waveform averaging and how the selected waveforms can be fitted to the averaged waveforms. Using the method of Rhomberg-Kauert et al. (2025), recorded waveforms can be averaged and used to outline general trends across a target (roof), which enables the subsequent comparison of the two selected initial waveforms, namely the Gaussian pulse and the heavy-tailed curve. Waveforms reflected from the same target, in this case the same roof, can be aligned by the first recorded sample, under the simplified assumption that the waveforms have the same phase. This provides multiple amplitudes, one from each waveform, for each sample interval, which can then be merged using the average across the amplitudes of each sample interval. The discrete representation of the averaged waveform of the target can then be interpolated to a continuous curve. To compare the Gaussian pulse and the heavy-tailed curve with these interpolated curves, the two pulses can be fitted to the data using least-square optimization, in this case using the SciPy (Virtanen et al. 2020) curve fitting module.

4.7 Ranging Based on Peak Detection

Lastly, to analyze the potential influence of the angle of incidence on the temporal position of the full-waveform maximum, we use the introduced homotopy (Eq. 25) to simulate different initial pulses. The primary analysis focuses on investigating the influence of the angle of incidence on the temporal position of the waveform maximum. In addition, the spectrum of waveforms allows us to analyze the influence of signal asymmetry for both the simulated waveform and the Gaussian fit of the same curve. This variation of different asymmetric waveforms and the difference between direct peak extraction and Gaussian fitting enables a further generalization, both highlighting the influence of the incidence angle, as well as providing insight how the assumed laser pulse shape influences the simulation.

For each simulated echo pulse, the peak can be extracted from the pulse without additional tools needed since the temporal resolution of our simulated waveform curves is arbitrarily high. For this, the simulation uses a 256-fold temporal resolution compared to the actual measurement rate of Sensor I, enabling a direct extraction of the time stamp of the maximum amplitude. The determined peak position on the temporal axis enables the comparison of each angle in an idealized setting, and thus the temporal change of the echo pulse peak. In addition, we can monitor the change related to the angle of incidence without accounting for noise. There, we measure two types of distance, the temporal shift of the pulse translated to distance and an idealized orthogonal distance, where we multiply the measured distance with the cosine of the input angle. This idealized orthogonal distance is selected as a secondary measure, as the theoretical temporal shift of the maximum amplitude would result in a shift along the laser shot direction. The shift would mostly be observed in plane-to-plane distances, which is approximated by the orthogonal distance.

For the analysis presented, it is important to note that we focus on peak detection applied directly to the simulated signal, as well as Gaussian pulses fitted to the simulated waveforms. This approach does not necessarily correspond to the classical target extraction methods used in measurement settings because the simulation is based on a higher sampling rate and is free of noise.

5 Results

This section is divided into three main parts. We present (i) the results of the simulation framework, outlined in Sect. 4.2, together with a comparison of the selected waveforms and real-world data (ii) the application of the simulated relation between the angle of incidence and the echo pulse with for real-world data, and (iii) the analysis of the

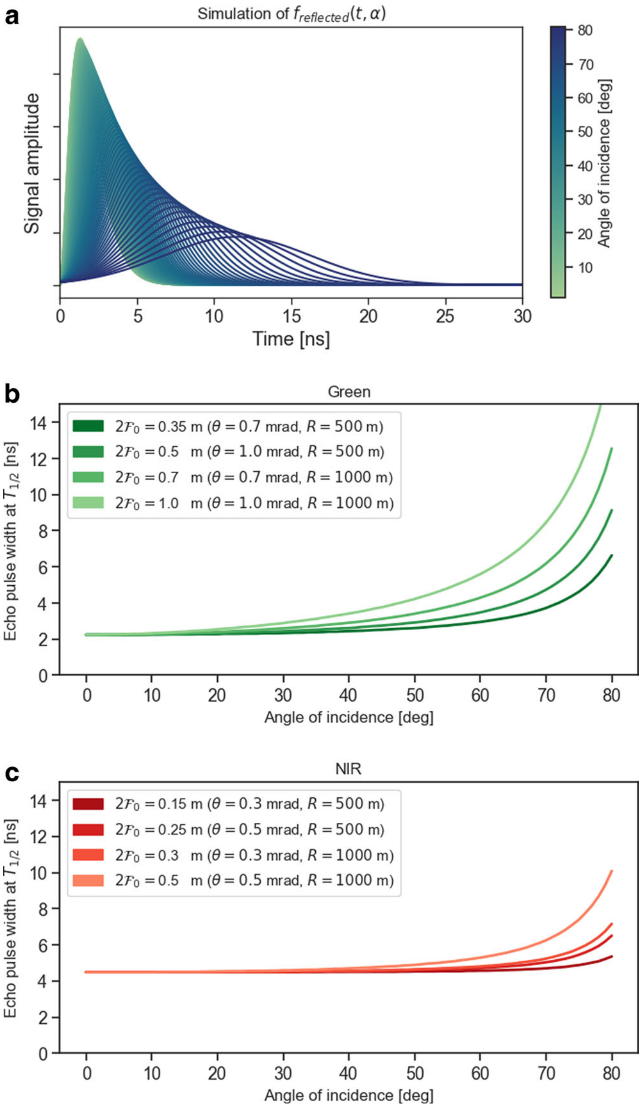

Fig. 6 **a** Simulated echo pulses based on our simulation outlined in Sect. 4.2 and the parameters of the green channels of System I, where $f_{\text{reflected}}(t, \alpha)$ is the convolution of the heavy-tailed curve *f*(*t*) and the differential backscattering cross section for the angled target $\widetilde{h}(t, \alpha)$. **b** Simulated curves for different settings of the green channel of System I **c** Simulated curves for different settings of the NIR channel of System I. For both (**b**) and (**c**) $2\mathcal{F}_0$ corresponds to the footprint diameter at ground level with zero incidence angle.

temporal shift of the maximum amplitude in relation to the angle of incidence and asymmetry of the initial laser pulse. For each part, different aspects are highlighted and a comprehensive analysis of the overall effect of the angle of incidence on the waveform is presented.

5.1 Relation of Echo Width and Angle of Incidence

Each curve simulated in Fig. 6a is based on the numerical convolution introduced in Sect. 4.2. In Fig. 6a, the simulation framework shows the change of the waveform shape with increasing angle of incidence. Both the decline in amplitude, aligned with the cosine law, and the widening of the pulse with increasing angle of incidence are clearly visible. The measured width for each input angle can then be plotted as a curve, which demonstrates the relation between the echo pulse width and the angle of incidence (Fig. 6). In Fig. 6b, the selected parameters represent the typical short laser pulse and medium-sized footprint common in bathymetric LiDAR in alignment with the green channel of System I, while Fig. 6c displays the simulated curves for the settings of the NIR channel of System I.

We observe that the curvature of the curve in Fig. 6b, c drastically increases at higher beam divergence or larger ranges. Both lead to an increase of the diameter of the laser footprint, which entails a clearly visible effect on the width of the returned echo pulse. The influence of the footprint size on the slope of the simulated curves can be seen in Fig. 6b, where the curves for the smallest and largest footprint differ significantly in curvature. The larger footprint leads to an earlier onset of the curvature, displaying a visible difference in echo pulse width at approximately 20—30°. In contrast, the longer pulse width and smaller footprint of the NIR channel lead to more moderately sloped curves, where doubling of the echo pulse width are not observed until high angles are reached (greater 70°), even for an exaggerated footprint diameter of e.g. 0.5 m at 0° angle of incidence (Fig. 6c).

5.2 Comparison of Different Waveforms

With the introduced waveform averaging, the two initially selected input curves for the simulation can be validated and provide insight if the selected laser pulse shapes adequately represent real-world. Here, the fitted functions are the heavy-tailed curve *f*(*t*) and the Gaussian pulse *g*(*t*). Depending on τ, amplitude and temporal position were optimized during fitting, using least squares optimization to match the averaged waveform (Fig. 7). In contrast to the simulation outlined in Sects. 4.2 and 4.5, these functions were chosen because common post processing similarly fits functions to the recorded waveform to extract target echoes. This also extends to the objective of this particular analysis, which focuses on comparing the two waveforms in terms of pulse symmetry and alignment with real-world data.

The alignment with the real-world data can be seen in Fig. 7. For the three selected roofs with varying slopes, in particular 10° (Fig. 7a, b), 20° (Fig. 7c, d) and 60° (Fig. 7e, f), an average waveform and a fitting of the selected input curves were calculated. In the panels A–D of Fig. 7, the echo pulse displays the standard initial peak followed by the ringing effect, which denotes artificial secondary echoes. For the 60° angles of incidence, the ringing

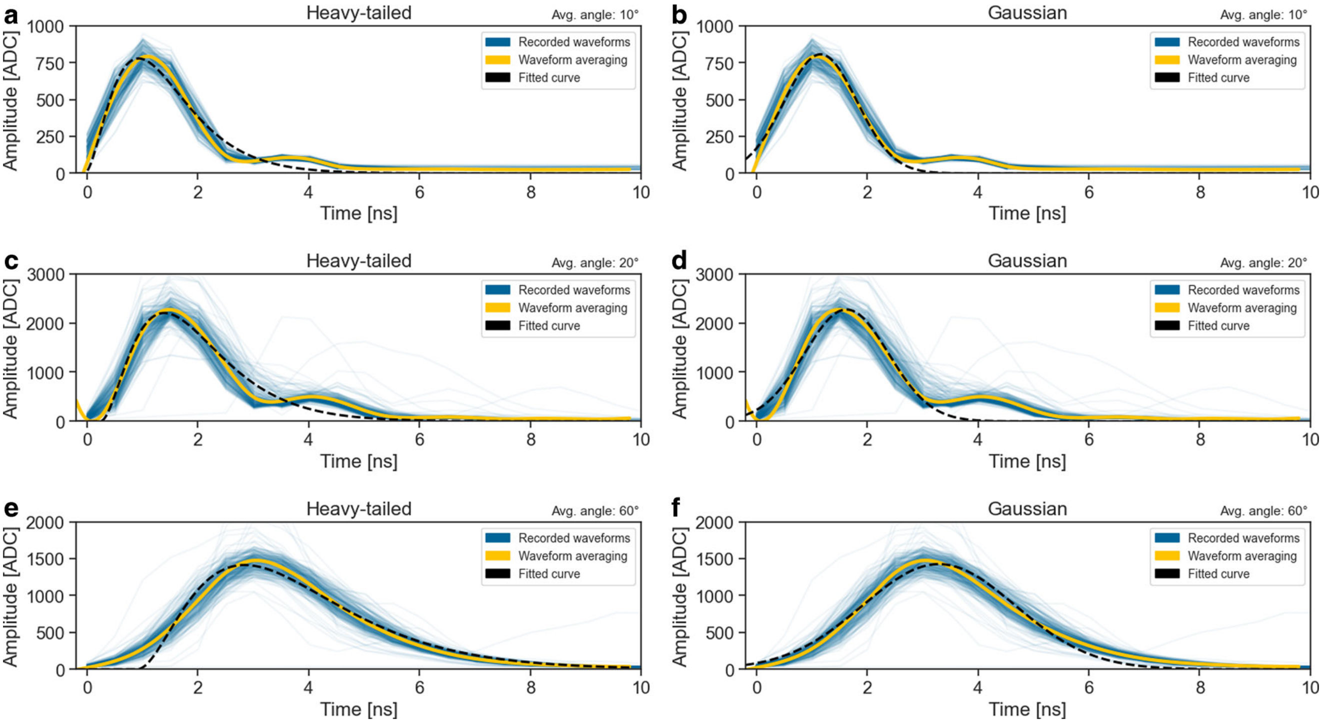

Fig. 7 Comparison of the heavy-tailed curve *f*(*t*) and the Gaussian pulse *g*(*t*) fitted to the averaged waveforms of three different roofs, where the angles of incidence for the roofs are 10° (**a** and **b**), 20° (**c** and **d**) and 60° (**e** and **f**). For each plot the blue waveforms are the recorded data. The yellow line is the interpolated averaged waveform and the dashed black line represents the fitted received laser pulse response.

effect merges with the echo pulse, causing a longer right-hand side of the pulse (Fig. 7e, f).

This is also where the two fittings of *f*(*t*) and *g*(*t*) deviate, as the heavy-tailed curve partially incorporates the ringing effect, and thus captures a more asymmetric shaped waveform. However, the Gaussian fitting mostly captures the initial peak of the echo pulse. Thus, the Gaussian pulse estimates a echo pulse width smaller than that of the heavy-tailed curve. In numbers, this translates to 1.66 ns, 1.55 ns and 1.61 ns (heavy-tailed, Gaussian and averaged waveform FWHM) for the 10° roof and 3.29 ns, 3.24 ns and 3.05 ns for the 60° roof. This outlines that both the heavy-tailed and Gaussian pulses deviate from the generalized echo pulse. However, comparing all panels of Fig. 7, the two selected input curves show a high alignment with the averaged waveforms and are able to capture the waveform shape with only minor deviations, for example, due to the ringing effect. Therefore, the selected curves provide a suitable foundation for the simulation and estimation of the angle of incidence, but future work could extend the simulation by incorporating real-world data or the system waveform of the laser scanner.

5.3 Angle Estimation

The previously introduced relation of the angle of incidence and echo pulse width can now be applied to the datasets of Sensors I and II. For the two datasets, the proposed estimation method is further compared with current best practices, namely the angle of incidence estimation with neighborhood-based surface normal vector calculations. The comparison between the two incidence angle estimation methods can be seen in Fig. 8.

Panels A and B of Fig. 8 show distribution plots (Kernel density estimation (KDE) plots) that present the alignment of the neighborhood-based and waveform-based angles of incidence for Sensor I and Sensor II, respectively. Panel C shows box plots of the evaluation metrics defined in Sect. 4.4. For Sensor I, the distribution shows an overall match around 50–60°, while the rest of the distribution shows a larger spread of the angles in the comparison (Fig. 8a). Sensor II displays larger discrepancies than Sensor I at incidence angles below 20°, with the incidence angles of both methods becoming more similar around 30–40°. Furthermore, the differences in point density, caused by the differences in pulse repetition rate, can also be seen in the distributions. Due to the differences in pulse repetition rate, Sensor I has a lower ground point density compared to Sensor II. Similarly, the differences in the scan pattern are also visible. Sensor I has a constant off-nadir scan angle, which in turn leads to higher angles of incidence than the linear scan pattern of Sensor II. Therefore, for the same area of interest, the incidence angles are lower for Sensor II than Sensor I.

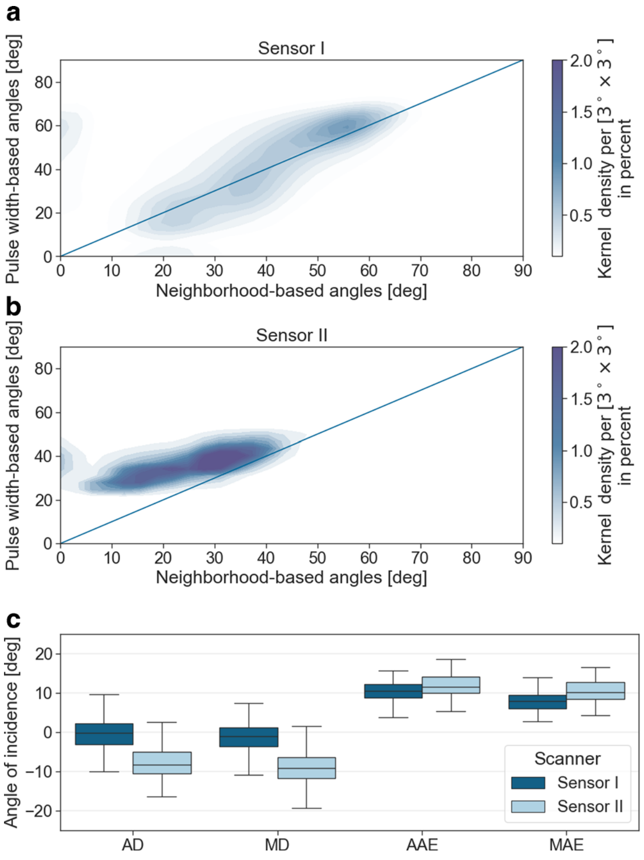

Fig. 8 **a** Kernel density estimation (KDE) plot of the neighborhood-based angles of incidence and echo pulse width-derived angles of incidence for the Sensor I dataset. The line of perfect fit is shown as the blue line across the plot. **b** Analogue KDE plot for the Sensor II dataset. **c** Evaluation of the differences between the echo pulse width and neighborhood-based angles of incidence, using the AD and MD as well as the AAE and MAE for the Sensor I and II dataset.

From a qualitative perspective, analysis of the data set from Sensor I reveals a high degree of similarity between the neighborhood-based and pulse width-based angles of incidence. The distribution shows a low degree of uncertainty, particularly for high angles of incidence (Fig. 8a). In comparison, the proposed method displays a less accurate performance for the Sensor II dataset (Fig. 8b). There, the pulse width-based angles of incidence overestimate the incidence angles compared to the neighborhood-based calculation.

On the quantitative side, the comparison of incidence angles for Sensor I has a spearman correlation of 0.52 and for Sensor II the spearman correlation is 0.53, showing similar results.

The differences in quantitative and qualitative results of Sensor I and Sensor II (Fig. 8a, b) can also be seen in Fig. 8c. There, the box-plots of the mean and median differences are centered around zero for Sensor I, while Sensor II shows a score close to 10°. These differences correspond to the deviations in the KDE plot from the line of perfect fit in Fig. 8a, b, while the quartiles display a similar extent underlining the similar correlation values. For Sensor II, the lower scores are related to the general overestimation of the angles of incidence (Fig. 8b). However, the mean and median absolute errors show similar results (Fig. 8a, b), which reflects similar spearman correlation, since the absolute values correspond to the differences of both distributions in the correlation analysis. Both datasets show a moderate correlation between pulse width-based angles and neighborhood-

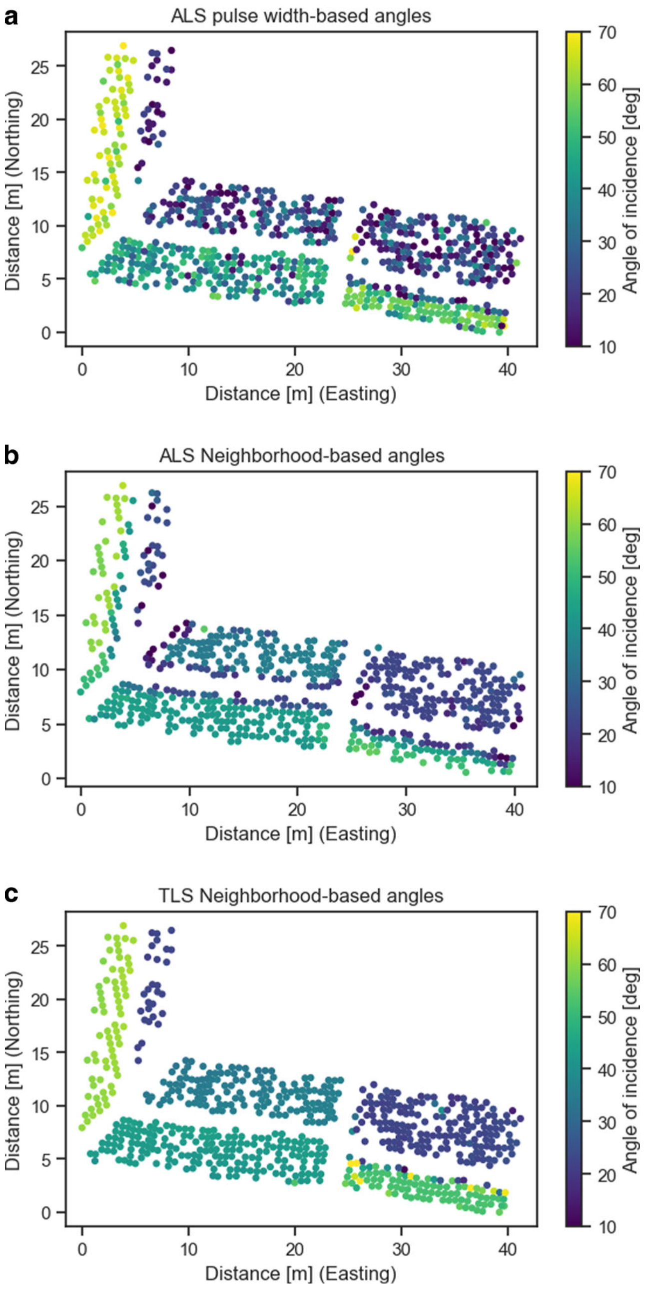

Fig. 9 Angles of incidence derived from terrestrial and airborne laser scanning (Sensor I). **a** ALS based on full-waveform analysis; **b** ALS based on normal vectors calculated with OPALS; **c** TLS angles based on normal vectors calculated with OPALS.

based angles, which aligns with the non zero absolute differences. The differences between the box plots can possibly be attributed to differences in the sampling rate and scanner setting, as well as to the different scan patterns. The non-constant off-nadir angle of the Sensor II scanner is one of those factors that might be responsible for the inflated estimation of the echo pulse width-based angles of incidence, similar to the different deviations from the line of perfect fit seen in the distribution shown in Fig. 8a, b.

5.4 Comparison to Terrestrial Laser Scan

The significantly higher density of the TLS point cloud can be used to improve the resolution of the neighborhood-based angle of incidence. Here, a search radius of 0.4 m and a point limit of 2500 neighboring points were selected for the same robust surface normal estimation using OPALS (Pfeifer et al. 2014). OPALS uses robust least squares adjustment for estimating the best fitting plane parameters, reducing the effect of outlier points on chimneys, antennas, or the like. The extracted incidence angles were then matched to the closest points of the ALS point cloud of Sensor I.

The visual comparison of the pulse width-based ALS incidence angles and the neighborhood-based TLS angles of incidence shows a good alignment for the roof on the left and right in Fig. 9a, c, while the roof in the center of the figure shows both matching and deviating angles of incidence. The angles derived for both datasets match well with the exception of the angles close to the roof ridge (Fig. 9b). This general alignment matches the KDE plots of Fig. 10. In panels A and B, both distributions are centered around the line of perfect fit. However, the distribution of Fig. 10a displays a larger deviation from the perfect fit line compared to Fig. 10b. Both distributions display similar characteristics in the center and a gap in the angles of incidence (Fig. 10a, b). This gap is caused by differences in roof orientation (Fig. 9).

The differences between the waveform-based estimation and the neighborhood-based workflow are also visible in the different types of deviation that both methods have (Fig. 9). The waveform-based estimation is sensitive to differences in the shape of the surface, causing distortions when the laser beam interacts with objects mounted on the roof (chimneys, dormers, etc.). This is, for example, the case for the easternmost house, as the solar panels are mounted on the south roof side and the north facing side features multiple smaller objects (Fig. 3c). In contrast, the ALS neighborhood-based angles deviate from the TLS neighborhood-based angles around the ridge line of the roofs, where the different faces of the roof intersect, and therefore the plane fitting performs poorly, due to the large footprint of the green channel of System I (Fig. 9).

Table 3 Median value of the scores shown in Fig. 9c. Average Difference (AD) and the Median Difference (MD), Average Absolute Error (AAE) and Median Absolute Error (MAE) for all point wise differences between the selected method and the angles of incidence extracted from the TLS.

Method	AD [deg]	MD [deg]	AAE [deg]	MAE [deg]
Waveform	0.59	7.40	13.03	10.55
Neighborhood	2.45	–2.71	6.83	2.12

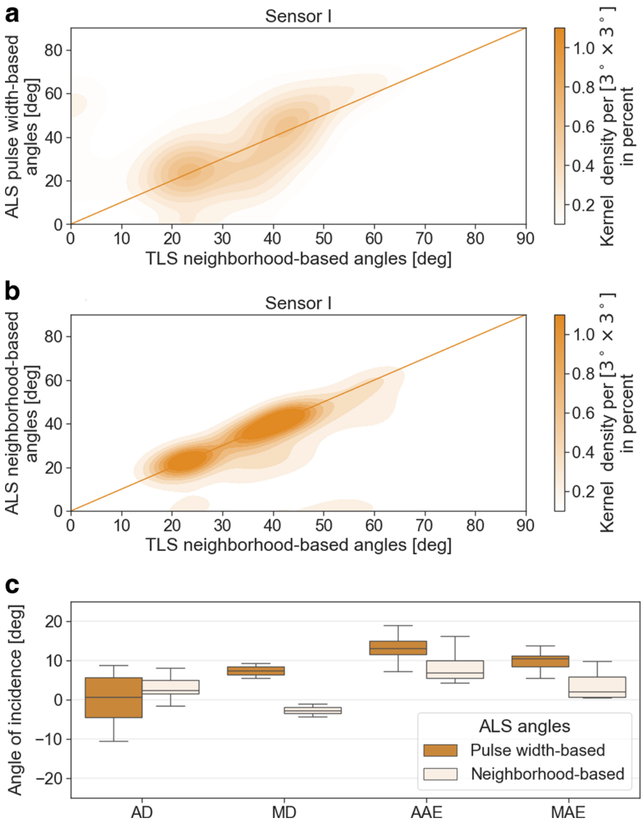

Fig. 10 **a** Kernel density estimation (KDE) plot of the ALS (Sensor I dataset) echo pulse width angles and TLS neighborhood-based angle of incidence. The line of perfect fit is shown as the orange line across the plot. **b** Analogue KDE plot for the neighborhood-based ALS and TLS angles. **c** Evaluation of the differences between the TLS neighborhood-based an and ALS angles of incidence, using the using the AD and MD as well as the AAE and MAE for the Sensor I.

Both datasets match for the center of the distributions, but display a difference at the tail of the distribution. Table 3 documents that the waveform-based estimation performs worse for most measures, except the average difference. In Fig. 9a the extracted incidence angles fluctuates, which corresponds to fluctuations in the underlying echo pulse width. Here, outliers in the waveform can potentially lead to an increase noise in the pulse width angles, which then corresponds to varying angles on the same roof. This in addition to the influence of differences in the roof material poses challenges to the presented method (Fig. 3c). For example,

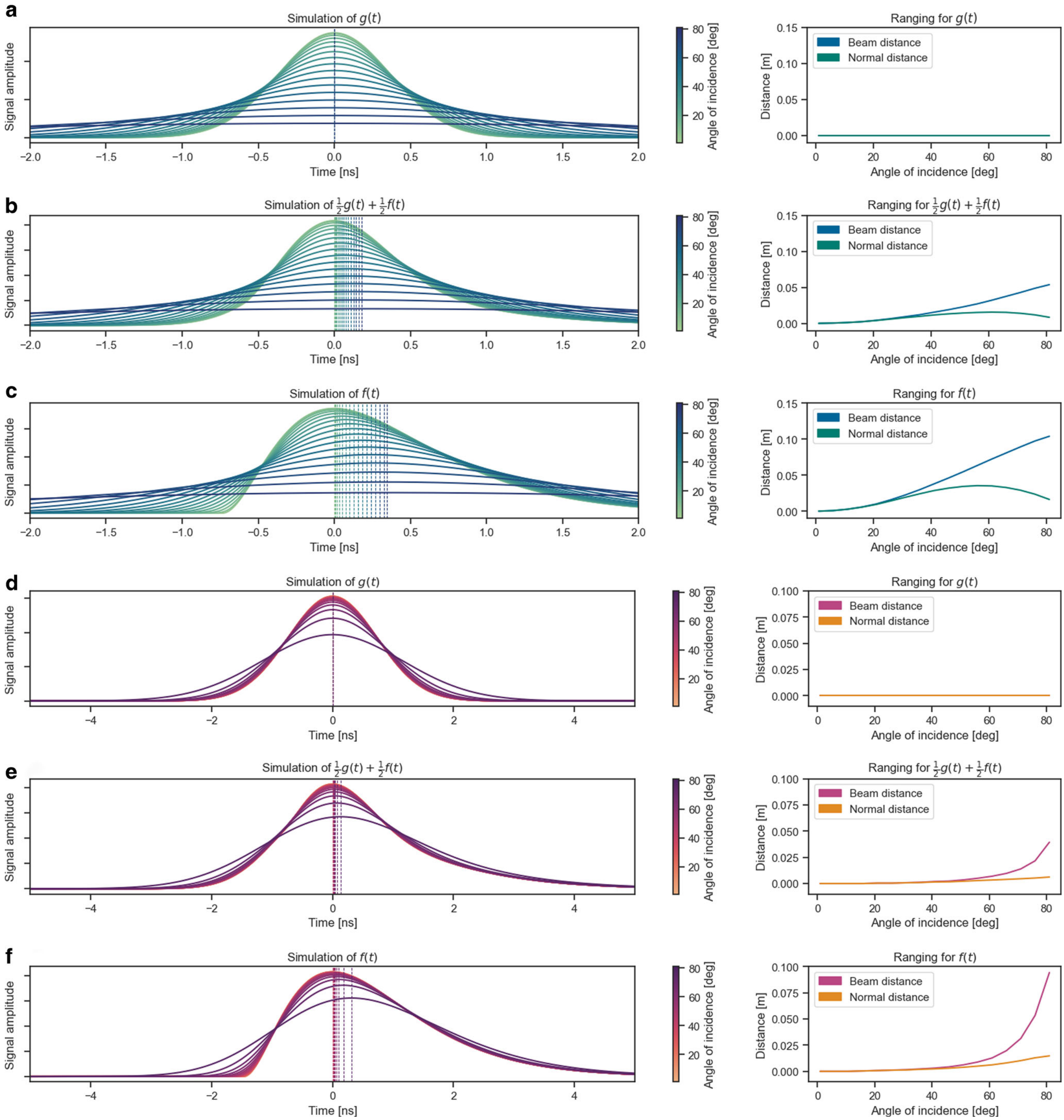

Fig. 11 Simulation of different possible echo pulses based on the Sensor I dataset. **a** Simulated LiDAR waveforms based on the convolution of a Gaussian pulse with the angle-dependent function and the associated ranging effects, for the parameters of the green channel. Each curve has the maximum amplitude marked (vertical line) and is colored by angle of incidence. The second second plot in the right column shows the associated shift of the maximum amplitude. **b** Combination of a Gaussian pulse and the heavy-tailed curve convoluted with the angle-dependent function, with the same ranging effect analysis. **c** Convolutions of the heavy-tailed curve with the angle-dependent function. **d**–**f** Analogous analysis of the first three panels with the NIR channel of Sensor I.

solar panels on the roof (Fig. 3c) would affect the reflected echo pulse, while flat constructions only marginally change neighborhood-based angles of incidence. In summary, the results shown in Fig. 10 show general similarity between the pulse width-based and neighborhood-based angle of incidence. The differences visible between the two angle of incidence methods are visible in the deviations of the KDE plots, where the methods vary in the density close to the perfect fit line (Fig. 10). The advantages of neighborhood-based incidence angles for planar surfaces can be seen in the inner region of the roofs (Fig. 9b), while deviations are observed on the roof ridge. The neighborhood-based angle of incidence estimation show a lower deviation from the TLS angles compared to the pulse width-based angles of incidence, but also in this case the alignment is not optimal (Fig. 10c).

5.5 Ranging Effects Based on Incidence Angle

In addition to the well-known change in the amplitude of the echo pulse, there is also a less distinct ranging bias observable at high angles of incidence. There, the pulse width and asymmetry of the waveform determine the shift of the waveform peak (Fig. 11).

The effects displayed in Fig. 11 illustrate the role of the waveform convoluted with the angle-dependent function. A Gaussian laser pulse (Fig. 11a, c) shows no temporal movement of the maximum amplitude, as the pulse is symmetrical and therefore no heavy-tailed part interacts with the angle-dependent function during the convolution. The other panels display the convolution of gradually more asymmetric curves with the angle-dependent function. In detail, the initial functions are either a homotopy $H(s,t)$ of a Gaussian pulse and the heavy-tailed curve or, alternatively, the heavy-tailed curve $f(t)$ itself. In both cases, a continued increase of the temporal offset, i.e. ranging bias, can be observed with increasing angle of incidence. This shift of the amplitude maximum towards a later point in time leads to an increase in the distance along the beam direction, which can be observed in the simulations of both the green and NIR channel of Sensor I. The influence of the beam divergence and the differences in FWHM can be seen in the shape of the curves in the ranging plots (Fig. 11). There, the short pulses and high beam divergence make the echo pulse more susceptible to the influence of the angle of incidence compared to the NIR channel of the same sensor. It is noted that the range does not necessarily correspond to the peak position, but a systematic effect is still visible in the simulation.

Furthermore, Fig. 11 shows the deviations for different angles of incidence for initial laser pulses with varying degree of asymmetry. There, the cosine function has a strong influence at higher angles of incidence and decreases the factually measured range biases when measured as orthogonal distance from the reflecting surface. In addition, we also applied Gaussian fitting to the simulated echo pulse for the extraction of the amplitude maximum. The main difference between both simulations is that fitting a Gaussian pulse produces less temporal shifts compared to the unfitted data, for example the maximum shift of the green channel is decreased from 10 to 5 cm for large angles of

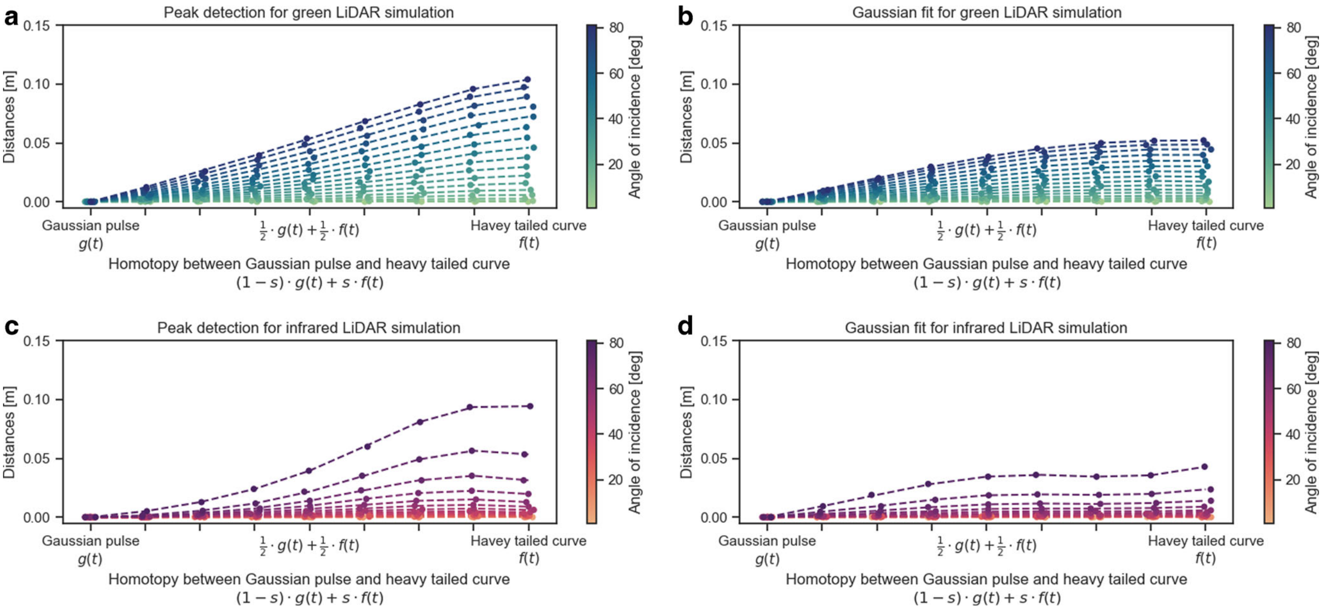

Fig. 12 Simulation of the temporal shift of the maximum amplitude for different simulated waveforms of Sensor I. The x-axes display different steps of the input homotopy between the Gaussian pulse and the heavy-tailed. **a** Convolutions of different input functions for pulses corresponding to the properties of the green LiDAR channel of Sensor I. Each ranging offset is colored by the angle of incidence. **b** Gaussian pulse fitting of the results of the convolutions. **c**, **d** The same analysis as in the first two panels applied to the NIR channel of Sensor I.

incidence, e.g. greater than 50° (Fig. 12a, b). Therefore, the simulated results show that there is a detectable distance effect depending on the initial waveform of the laser pulse and the fitted function during peak detection.

5.6 Influence of Echo Pulse Symmetry

The difference in symmetry of the echo pulse has an influence on the temporal position of the maximum amplitude (Fig. 11). The shifts are visible in the simulated echo pulse but, as processing often applies Gaussian fitting, the differences might partially be decreased by the fitting of a symmetric waveform. Therefore, the analysis uses homotopy curves to simulate different degrees of symmetry and further analyzes the influence of Gaussian fitting on the changes in the temporal shift (Fig. 12). To fully analyze these influences, the waveforms are simulated with 256-fold temporal resolution and waveform parameters as reported in Table 2 for the green component of Sensor I. There, the temporal shift of the maximum amplitude changes when moving away from the symmetric Gaussian pulse and toward the heavy-tailed curve (Fig. 12b). This effect is due to the convolution with the asymmetric part of the distribution, as this asymmetry delays the maximum amplitude, which in turn corresponds to a stronger ranging bias with increasing angles of incidence. This emphasizes the importance of the appropriate waveform model when considering range effects that are related to the angle of incidence in real data.

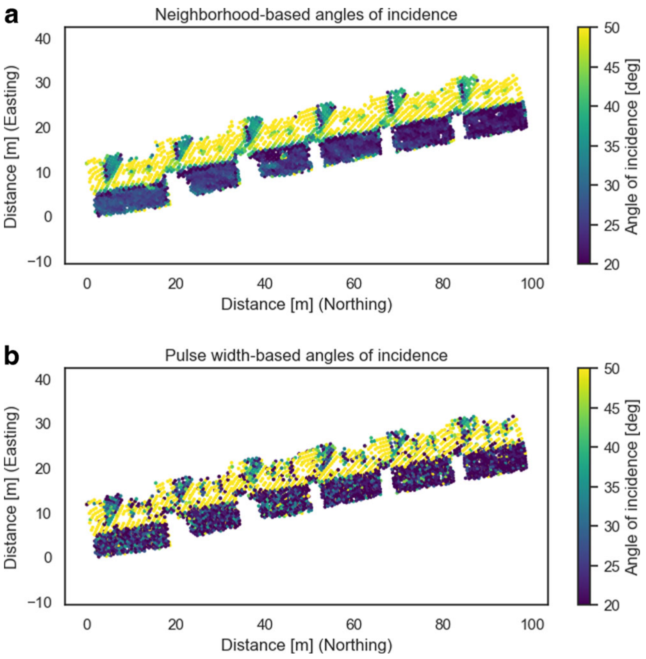

Fig. 13 Plan view of a selected subset of roofs from the Sensor I dataset. **a** Colored by the angles of incidence derived from beam direction and surface normal vectors. **b** Colored by the angles of incidence based on the proposed estimation method.

It also highlights that an estimate of the incidence angle can improve laser range estimation, especially for pulses with short duration and large beam divergence.

6 Discussion

Our simulation framework helps to investigate a wide spectrum of applications, ranging from the incidence angle estimation to the analysis of potential range biases. The results display an overall applicability of the proposed waveform-derived angles, but also outline challenges for the new method. For the ranging analysis, the results presented remain purely theoretical. Thus, a critical discussion of the results in light of established research is presented in the following.

6.1 Angle Estimation

In Sect. 4, we introduced a new method to estimate the angles of incidence based on individual laser waveforms. When comparing the results of this method with current standard practices, both methods face distinct challenges (Fig. 13). Similarly to neighborhood-based methods profiting from higher point densities, a higher waveform sampling rate would potentially improve waveform fitting and thus improve waveform-based angle estimation. For neighborhood-based plane fitting with optimized parameters, more supervision might be required, which deceases autonomous processing.

In addition, real-world data is generally more prone to local variation in texture and reflectance, as difference in exposition causes inhomogeneous deterioration of material. This could be addressed through laboratory experiments. Therefore, future work might include data testing in a controlled laboratory environment, which is outside the scope of this study.

For the proposed angle-of-incidence estimation method, the accuracy of the estimation improves with a larger beam divergence or longer measurement range. This is due to the fact that relative changes in the echo pulse width become more detectable (Sect. 5.1). The relation of absolute and relative change in echo pulse width under those conditions exceeds measurement inaccuracies, allowing each echo pulse width to be distinctly matched to an angle of incidence.

This contrasts previous work, which focused on NIR LiDAR system with long pulses and small footprint and presented no clear relation between the echo pulse width and the angle of incidence for the NIR LiDAR system (Pfennigbauer et al. 2013). However, the results in this study build on the difference in laser pulse shape, namely the shorter pulse and larger footprint diameter. For these initial laser pulses, the recorded echo pulse width displays a larger relative change at smaller angles of incidence, and thus a relation between the two quantities can be established and applied to real-world data. To increase the accuracy of the method w.r.t. detecting minimal changes in echo pulse width, higher receiver bandwidths and sampling rates would be required. Therefore, in certain cases, existing methods based on surface normal estimation, e.g., using OPALS (Pfeifer et al. 2014) may yield better results. However, in all applications with medium footprints and short pulses, the new method offers the possibility of estimating a neighborhood-independent angle of incidence, which improves current best practices by eliminating the parameterization of the neighborhood selection process.

6.2 Comparison Based on TLS Data

Comparison of both methods with the TLS data allows us to estimate the performance of both the ALS neighborhood-based method and the proposed method. The general comparison of both methods using the point-wise comparison shows that the ALS angles based on the point neighborhood yield better results for the selected roofs (Fig. 10). For the TLS data set, the partial obstruction of the southward roof with solar panels and smaller objects sets suboptimal conditions for the echo pulse width-based estimation. Therefore, the neighborhood-based method displays expected advantages which would decrease for curved surfaces or lower point densities. In conclusion, the newly introduced method is able to estimate angles of incidence quite well, showing a general alignment compared to current best practices. It has to be noted that compared to high resolution (e.g. TLS) data, neighborhood-based method outperforms the pulse width-based angle of incidence method. However, the advantage of extracting the angle of incidence information using the echo pulse width is that this can be done directly from the recorded waveform, and thus no additional processing is required.

6.3 Influence of Beam Divergence and Pulse Width

The variance in the appearance of the relation between the width of the echo pulse and the angle of incidence outlined in Sect. 5.1 explains why the estimation of the incidence angles based on the width of the echo pulse has not been quantified in previous research (Pfennigbauer et al. 2013). There, small beam divergence and typical airborne measurement distances of several hundred meters, in combination with a long initial pulse width, make the relative change barely noticeable at low angles less than 30° (Fig. 6). This especially extends to even smaller footprints in typical NIR LiDAR. Therefore, in cases of low beam divergence or close-range scanning applications, the relative change of the echo pulse width would hardly be detectable with standard laser scanning devices, and precise matching to the angle of incidence would therefore fail.

Furthermore, the functions that are used to describe the echo pulse have a non-neglectable impact on the estimated FWHM as seen in Fig. 7. There, the focus on the theoretical framework diverges in the expected FWHM and calculated FWHM, as the laser class of the different systems would suggest a 1.5 ns FWHM for the green channel and 3 ns for the NIR channel, while the simulation starts at 2.2 ns and 4.5 ns respectively. This difference in pulse width is not unexpected, as the reflected echo pulse is already a convolution of the unknown pulse emitted by the LiDAR system and the interaction with the target (Wagner et al. 2006). However, the comparison with real-world data (Fig. 7) shows a lower increase than the output of the simulation. There, factors such as function or parameter selection have a large influence on the initial starting point; one larger factor not taken into account is the asymmetric change in footprint size with target inclination, which at this point remains future work. During the application of the simulation to real-world data, the pulse-width-based incidence angles display an overall alignment with the neighborhood-based angles of incidence, hence supporting the theoretical model of the simulation. While we use NIR and green laser pulses of the presented scanners for our study, they rather serve as role models for systems with long pulse duration and small beam divergence (NIR) and short pulse duration and larger beam divergence (green), respectively. In fact, the findings presented in this study are not related to the laser wavelength, but the applicability of the presented method only depends on the duration-width ratio of the emitted laser pulses (Wagner et al. 2006). Therefore, the two wavelengths commonly differ in laser scanning parameters, but the differences in simulated recorded full-waveforms do not correspond to the wavelength itself.

In conclusion, the application of the proposed estimation method requires a certain minimum laser footprint to be practically viable. Our proposed method is therefore better suited for topo-bathymetric LiDAR sensors employing short (1.5 ns) but broad (1 mrad) pulses compared to LiDAR devices used for topographic mapping, which typically employ narrow beams (0.2 mrad) and longer pulse duration (3 ns). However, our method also has potential for future improvements through empirical data or more advanced simulations.

6.4 Ranging Effects

The ranging effects outlined in Sect. 5.5 reveal new insights related to hypothesized range biases for large footprint LiDAR systems (Roca-Pardiñas et al. 2014). The analysis shows a temporal shift of the waveform peak for increasing angles of incidence. The analyzed phenomenon is again related to the width (duration) of the emitted laser pulse. A shorter pulse creates stronger artifacts at lower angles of incidence. In all cases, the symmetry of the Gaussian pulse model means that no range bias occurs. As the initial waveform, emitted by the LiDAR system, is more accurately described as an asymmetrical waveform or a heavy-tailed curve, more appropriate waveform models than the Gaussian model should be selected as input for the simulation (Chauve et al. 2007; Pfennigbauer et al. 2013). The evaluation of the effects that arise from asymmetric waveforms during measurements poses multiple challenges. First, the fitting of the waveform, which can reduce the asymmetry of the waveform and thus reduce the temporal shift of the peak (Fig. 12). Secondly, the reference data (comparison of the normal distance between two planes) can only be obtained for flat targets, where the effect is observed only orthogonally to the reference surface and a large angle of incidence reduces the measured normal distance (Fig. 11). Finally, there are few available waveform samples across the short echo pulses often deployed by bathymetric LiDAR, posing a limitation to the waveform resolution. Therefore, a clear quantification of the simulated ranging offset would presumably be observed under laboratory conditions (Castorena and Creusere 2015; Li et al. 2018, 2020; Mechelke et al. 2007). For example, the work of (Mechelke et al. 2007) investigated such effects and presented insights on range accuracy related to the angle of incidence and furthermore outlined that the color of the target also influences the measurement accuracy. Therefore, future work should also address non Lambertian reflectors to extend the simulation to incorporate such investigation.

7 Conclusion

The study presents a framework to simulate the interaction of a laser pulse with an angled target. The simulation is used to establish a relation between the angle of incidence and echo pulse width, which allows to estimate neighborhood-independent angles of incidence. Furthermore, the simulation is used to analyze the effect of angled target on range measurements.

7.1 Angle of Incidence Simulation

Through the simulation introduced, we were able to present a new method of estimating angles of incidence based on full-waveform data. We applied the new method to real-world data and furthermore analyzed shifts of the maximum amplitude in relation to the incidence angle. Thus, we introduced an approach for the calculation of the angle of incidence that is independent of the local neighborhood. For the analysis of potential ranging artifacts, we have employed different pulse models (Gaussian pulse and heavy-tailed curve) and laser pulse parameters (beam divergence and pulse duration) and shown possible offsets, which remain to be tested in a laboratory environment, in future work.

The angle of incidence estimation has been shown to work best for relatively short pulses (1.5 ns) and broad laser footprints (1 mrad), typically used for the green channel of topo-bathymetric laser scanners.

7.2 Ranging Effects

In addition, numerical simulation for the analysis of range effects related to the angle of incidence has shown a theoretical bias. This theorized bias is hard to quantify from real-world data alone, and thus future work with high-accuracy references would be required. In general, laser pulses with a higher degree of asymmetry suffer more than strictly symmetric pulses, as is the case for a Gaussian pulse. Our findings form a basis for future studies to improve the accuracy of LiDAR data derived from full-waveform analysis in real-world scenarios.

7.3 Summary

In conclusion, our work offers a novel approach for extracting angles of incidence from full-waveform LiDAR data. Together with the new insights from the improved simulation framework, this builds a general foundation to advance the understanding of laser pulse interaction with inclined targets and therefore provides a robust foundation for future work.

Funding The authors acknowledge TU Wien Bibliothek for financial support through its Open Access Funding Programme.

Funding Open access funding provided by TU Wien (TUW).

References

Allouis T, Bailly J-S, Pastol Y, Le Roux C (2010) Comparison of LiDAR waveform processing methods for very shallow water bathymetry using raman, near-infrared and green signals. Earth Surf Process Landforms 35(6):640–650

Arkowitz M (2011) Introduction to homotopy theory. Springer

Bolkas D (2019) Terrestrial laser scanner intensity correction for the incidence angle effect on surfaces with different colours and sheens. Int J Remote Sens 40(18):7169–7189

Bundesamt für Eich- und Vermessungswesen (2024) Austrian map online. https://www.bev.gv.at/Services/Produkte/Austrian-Map/Austrian-Map-online.html

Carlsson T, Steinvall O, Letalick D (2001) Signatur simulation and singal analysis for 3-D laser radar. FOI-R-0163-SE. FOI—Swedish Defence Research Agency, Linköping, p 57

Castorena J, Creusere CD (2015) Sampling of time-resolved full-waveform LiDAR signals at sub-nyquist rates. IEEE Trans Geosci Remote Sens 53(7):3791–3802

Chauve A, Mallet C, Bretar F, Durrieu S, Pierrot-Deseilligny M, Puech W (2007) Processing full-waveform LiDAR data: modelling raw signals. ISPRS Workshop Laser Scanning Silvilaser 36(Part 3/W52):102–107

Guo Q, Su Y, Hu T (2023) Working principles of LiDAR. Elsevier, pp 23–61

Hartzell PJ, Glennie CL, Finnegan DC (2015) Empirical waveform decomposition and radiometric calibration of a terrestrial full-waveform laser scanner. IEEE Trans Geosci Remote Sens 53(1):162–172

Hu Y, Hou A, Ma Q, Zhao N, Xu S, Fang J (2022) Analytical formula to investigate the modulation of sloped targets using LiDAR waveform. IEEE Trans Geosci Remote Sens 60:1–12

Ji X, Yang B, Wang Y, Tang Q, Xu W (2022) Full-waveform classification and segmentation-based signal detection of single-wavelength bathymetric LiDAR. IEEE Trans Geosci Remote Sens 60:1–14

Kaasalainen S, Jaakkola A, Kaasalainen M, Krooks A, Kukko A (2011) Analysis of incidence angle and distance effects on terrestrial laser scanner intensity: search for correction methods. Remote Sens 3(10):2207–2221

Kukko A, Kaasalainen S, Litkey P (2008) Effect of incidence angle on laser scanner intensity and surface data. Appl Opt 47(7):986

Laconte J, Deschenes S-P, Labussiere M, Pomerleau F (2019) LiDAR measurement bias estimation via return waveform modelling in a context of 3D mapping. In: 2019 International Conference on Robotics and Automation(ICRA). Institute of Electrical and Electronics Engineers (IEEE), pp 8100–8106

Li Y, Ibanez-Guzman J (2020) LiDAR for autonomous driving: the principles, vhallenges, and trends for automotive LiDAR and perception systems. IEEE Signal Process Mag 37(4):50–61

Li X, Yang B, Xie X, Li D, Xu L (2018) Influence of waveform characteristics on LiDAR ranging accuracy and precision. Sensors 18(4):1156

Li X, Liu C, Wang Z, Xie X, Li D, Xu L (2020) Airborne LiDAR: state-of-the-art of system design, technology and application. Meas Sci Technol 32(3):32002

Ma X, Jiang H, Jin X (2024) Asymmetric gaussian echo model for LiDAR intensity correction. Remote Sens 16(24):4625

Mallet C, Bretar F (2009) Full-waveform topographic LiDAR: State-of-the-art. ISPRS J Photogramm Remote Sens 64(1):1–16

Mandlburger G (2020) A review of airborne laser bathymetry for mapping of inland and coastal waters. Hydrogr Nachr 116:

Mandlburger G, Pfennigbauer M, Steinbacher F, Pfeifer N (2011) Airborne hydrographic LiDAR mapping-potential of a new technique for capturing shallow water bodies. In: Proceedings of the 19th International Congress on Modellingand Simulation Perth, pp 12–16

Mandlburger G, Pfennigbauer M, Schwarz R, Pöppl F (2023) A decade of progress in topo-bathymetric laser scanning exemplified by the pielach river dataset vol X-1/W1. International Society for Photogrammetry and Remote Sensing, pp 1123–1130

Mechelke K, Kersten TP, Lindstaedt M (2007) Comparative investigations into the accuracy behaviour of the new generation of terrestrial laser scanning systems. Proc Opt 3:19–327

Nelson R (2013) How did we get here? An early history of forestry LiDAR. Can J Remote Sens 39(sup1):S6–S17

Pfeifer N, Mandlburger G, Otepka J, Karel W (2014) OPALS—a framework for airborne laser scanning data analysis. Comput Environ Urban Syst 45:125–136

Pfennigbauer M, Ullrich A (2011) Multi-wavelength airborne laser scanning. In: Proceedings of the International LiDAR Mapping Forum. ILMF, New Orleans

Pfennigbauer M, Wolf C, Ullrich A (2013) Enhancing online waveform processing by adding new point attributes. In: Turner MD, Kamerman GW (eds) Laser RadarTechnology and Applications XVIII SPIE.

Pfennigbauer M, Wolf C, Weinkopf J, Ullrich A (2014) Online waveform processing for demanding target situations. In: Laser Radar Technology and Applications XIX; and AtmosphericPropagation XI SPIE. vol 9080, pp 142–151

Rhomberg-Kauert J, Pöppl F, Pfennigbauer M, Mandlburger G (2024) Estimation of the angle of incidence based on echo pulse width in airborne LiDAR. Wissenschaftlich-Technische Jahrestagung der DGPF. Beiträge: 44, vol 32, pp 67–76

Rhomberg-Kauert J, Himmelsbach T, Pöppl F, Dammert L, Pfennigbauer M, Mandlburger G (2025) Mapping river topography in whitewater rapids using bathymetric LiDAR

RIEGL, Laser Measurement Systems (2022a) *RIEGL* VQ-1560i-DW datasheet

RIEGL, Laser Measurement Systems (2022b) *RIEGL* VQ-880-GII datasheet

Roca-Pardiñas J, Argüelles-Fraga R, de Asís López F, Ordóñez C (2014) Analysis of the influence of range and angle of incidence of terrestrial laser scanning measurements on tunnel inspection. Tunn Undergr Space Technol 43:133–139

Schwarz R, Pfeifer N, Pfennigbauer M, Ullrich A (2017) Exponential decomposition with implicit deconvolution of LiDAR backscatter from the water column. J Photogramm Remote Sens Geoinfo Sci 85:159–167

Schwarz R, Mandlburger G, Pfennigbauer M, Pfeifer N (2019) Design and evaluation of a full-wave surface and bottom-detection algorithm for LiDAR bathymetry of very shallow waters. ISPRS J Photogramm Remote Sens 150:1–10

Synge E (1930) Xci. a method of investigating the higher atmosphere. Lond Edinb Dublin Philos Mag J Sci 9(60):1014–1020

Ullrich A, Pfennigbauer M (2011) Echo digitization and waveform analysis in airborne and terrestrial laser scanning. In: Photogrammetric week, vol 11, pp 217–228

Ullrich A, Studnicka N, Hollaus M, Briese C, Wagner W, Doneus M, Mücke W (2007) Improvements in dtm generation by using full-waveform airborne laser scanning data vol 6, pp 2007–2007

Virtanen P, Gommers R, Oliphant TE, Haberland M, Reddy T, Cournapeau D, Burovski E, Peterson P, Weckesser W, Bright J, van der Walt SJ, Brett M, Wilson J, Millman KJ, Mayorov N, Nelson ARJ, Jones E, Kern R, Larson E, Carey CJ, Polat İ, Feng Y, Moore EW, VanderPlas J, Laxalde D, Perktold J, Cimrman R, Henriksen I, Quintero EA, Harris CR, Archibald AM, Ribeiro AH, Pedregosa F, van Mulbregt P (2020) SciPy 1.0: fundamental algorithms for scientific computing in python. Nat Methods 17:261–272 (SciPy 1.0 Contributors)

Wagner W (2010) Radiometric calibration of small-footprint full-waveform airborne laser scanner measurements: basic physical concepts. ISPRS J Photogramm Remote Sens 65(6):505–513

Wagner W, Ullrich A, Ducic V, Melzer T, Studnicka N (2006) Gaussian decomposition and calibration of a novel small-footprint full-waveform digitising airborne laser scanner. ISPRS J Photogramm Remote Sens 60(2):100–112

Wang C, Li Q, Liu Y, Wu G, Liu P, Ding X (2015) A comparison of waveform processing algorithms for single-wavelength LiDAR bathymetry. ISPRS J Photogramm Remote Sens 101:22–35

Williams GM Jr (2017) Optimization of eyesafe avalanche photodiode LiDAR for automobile safety and autonomous navigation systems. Opt Eng 56(3):31224

Yang T, Lai J, Wang C, Yan W, Ji Y, Zhao Y, Wu Z, Li Z (2021) Influence of a target's inclination on LiDAR waveform and its application. IET Optoelectron 16(1):27–33